

Experimental analysis of the wake of a horizontal-axis wind-turbine model



L.E.M. Lignarolo^{a,*}, D. Ragni^a, C. Krishnaswami^a, Q. Chen^{a,b}, C.J. Simão Ferreira^a, G.J.W. van Bussel^a

^a Delft University of Technology, Wind Energy, Delft, The Netherlands

^b State Key Laboratory of Water Resources and Hydropower Engineering Science, Wuhan University, Wuhan, China

ARTICLE INFO

Article history:

Received 12 September 2013

Accepted 13 January 2014

Available online 24 February 2014

Keywords:

Horizontal axis wind turbines

Wind turbine wake

Tip vortex breakdown

Wake instability

Wake re-energising

Wake mixing

ABSTRACT

The wake of a wind turbine is the driving phenomenon for energy recovery in a wind farm and for the interaction between wind turbines. The vortical structures of the wake of a horizontal-axis wind-turbine model are investigated in the Open Jet Facility wind-tunnel of Delft University of Technology. Velocity fields are acquired with stereoscopic particle image velocimetry, both unconditionally sampled and phase-locked with the blade motion, allowing for a statistical analysis of the mixing process of the wake, distinguishing between the contribution of the organised periodic motions and the random turbulent fluctuations. The evolution of the wake is measured up to five diameters downstream of the model. The stream-wise development of the wake velocity, pressure and total enthalpy of the flow is determined. Results show that the wake instability caused by the pair-wise interaction of the blade tip-vortices (so called “leapfrogging phenomenon”) has a strong impact on the momentum deficit recovery of the wake, by enhancement of the mixing process downstream of the tip-vortex helix instability, where the contribution of the random fluctuations becomes predominant. The experimental data are made available online together with a complete description of the wind turbine model.

© 2014 Elsevier Ltd. All rights reserved.

1. Introduction

The wake of a horizontal axis wind-turbine (HAWT) is a region of three-dimensional turbulent flow characterised by a deficit of kinetic energy and a complex vortical helical structure. Although several experimental and numerical analysis have demonstrated the link between the momentum deficit in the turbine wake and the rotor performance (see the works of [18,21,24]), an accurate prediction of the wake characteristics such as the recovery length and the expansion rate still is unfeasible, especially when considering wind-farm applications where multiple wakes are produced by arrays/clusters of turbine rotors. The large inaccuracies encountered in the numerical prediction of the kinetic energy recovery are typically associated with a poor modelling of the wake (see Ref. [2] and of the turbine loads, generally based on actuator disc or actuator line models. As shown by Ref. [17]; the actuator disc model in combination with the $k-\epsilon$ turbulence model produce a

strong region of high turbulence close to the blade, quickly decaying in proximity of the turbine model, as shown in Ref. [17]. The presence of this region is primarily artificial and in disagreement with in-field experimental observations [13], showing that a consistent turbulent mixing persists up to the turbine far wake. The effect of the incorrect representation of the wake re-energising mechanisms is confirmed by the large dispersion of current CFD results in the prediction of wind-farm power by different turbulence models, as in Ref. [22].

Refs. [3,9] showed how in large wind farms, the wake energy recovers via entrainment of kinetic energy from the flow surrounding the farm. The kinetic energy entrainment occurs at two different scales: the atmospheric turbulent flow level and the wake-induced flow level. The second one is of particular interest because it concerns the mixing process owing to the presence of the tip vortex helix, its instability and its breakdown, which are directly dependent on the turbine design and operation and on the interaction among multiple turbines and wakes. This is even more relevant for off-shore wind farms, where atmospheric turbulence is lower than on-shore.

Few studies focus on the self-induced mixing of the wake. Refs. [8,11,21] showed the influence of different parameters (such

* Corresponding author.

E-mail address: l.lignarolo@tudelft.nl (L.E.M. Lignarolo).

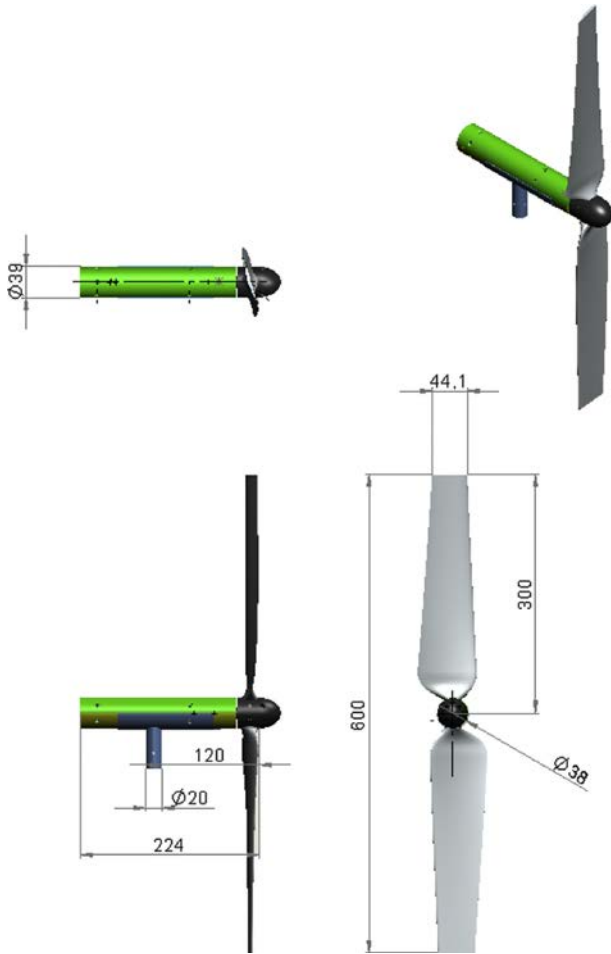


Fig. 1. Wind turbine model. Dimensions are in millimetres.

as tip-speed ratio, inflow turbulence, tip-vortex core size) on the stability properties of the wake. Ref. [13]; in contradiction with previous statements of [10]; hypothesized that the near wake tip-vortices inhibit the wake mixing and the outer air entrainment;

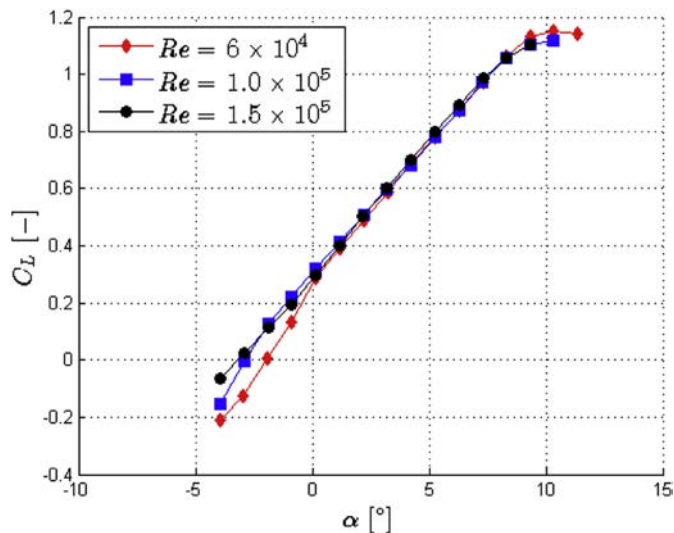


Fig. 2. C_L - α curves of airfoil E387 from $Re = 0.6$ to $Re = 1.5 \cdot 10^5$.

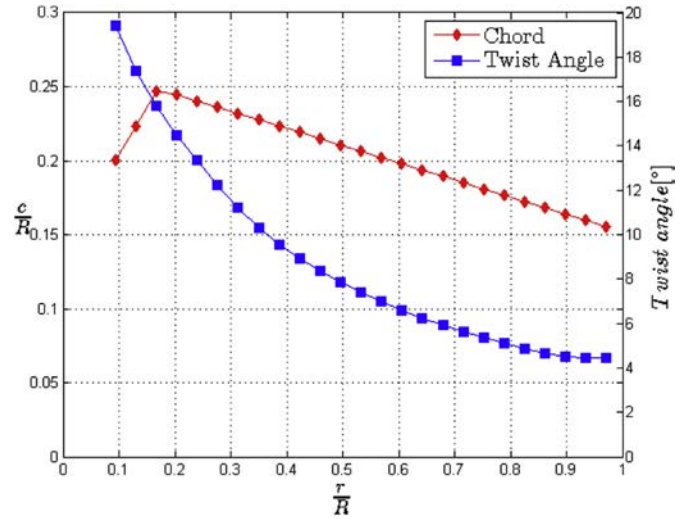


Fig. 3. Chord-radius ratio and twist-angle distribution of the wind-turbine model blades.

however, this hypothesis is presented without a clear quantification of the effect of the vortices and their break-down on the mixing process. Ref. [9] demonstrates the importance of the vertical transport of kinetic energy to replenish the wake, analysing the mixing process due to the large scale atmospheric turbulence and its effect on the smaller scale flow structures within a wind farm. Refs. [20,24] experimentally studied the dynamics of the turbulent mixing in the wake of perforated discs as simulation of an actuator disk.

In the present manuscript, a detailed measurement and analysis of the vortical structures in the wake of a HAWT is performed with stereoscopic particle image velocimetry (SPIV), in order to visualise the dependency between the wake re-energising process and the tip-vortex helix development, in the near and far wake of the turbine. The wake velocity field is measured up to 5 diameters downstream. The different measurements are acquired with both phase-locked and unconditioned sampling techniques, respectively by triggering the acquisition system in phase with the rotor and randomly. The complete statistical representation of the phase-averaged and mean flow allows for the distinction between the contributions of the random fluctuation and the organised periodic fluctuations in the mixing process of the wake with the outer flow. A series of measurement with a six-

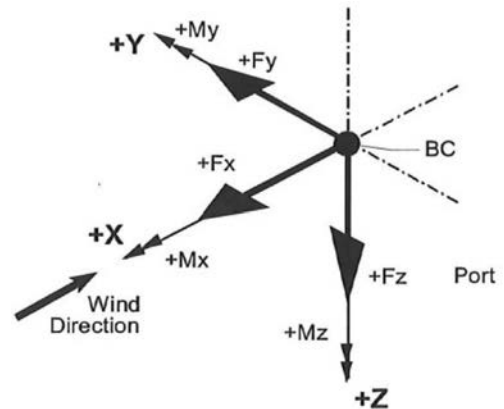


Fig. 4. Reference system for the balance measurements.

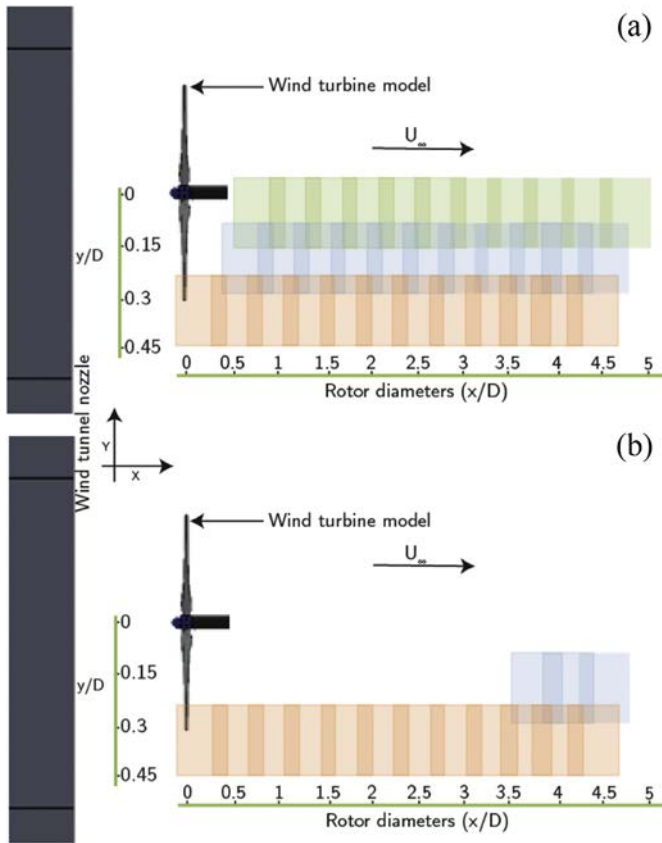


Fig. 5. Schematics of the field of views employed for phase-locked analysis (a) and unconditioned sampling one (b).

component balance is performed for obtaining the thrust coefficient curve of the wind turbine model.

In the next section of this paper, all of the information about the wind tunnel characteristics, the experimental set-up and wind turbine model is given. In the third section results are presented and discussed. The last section contains the conclusions.

2. Experimental set-up

2.1. Wind-tunnel and turbine model

The experimental study has been conducted in the closed-loop open-jet wind-tunnel of the Delft University of Technology (TU Delft). The wind-tunnel has an octagonal nozzle with a 3 m equivalent diameter and a contraction ratio of 3:1. The wind tunnel is powered by a 500 kW fan and can achieve a maximum velocity of 34 m/s at the test section. The free-stream flow at the measurement location has a turbulence intensity of 0.5%. The free-stream area contracts with a 4.75° semi-angle along the length of the jet, due to the development of the jet shear layer. The flow temperature is kept constant at 20 °C by a heat exchanger which provides up to 350 kW of cooling power. Details on the open-jet stability up to five turbine diameters are

Table 1
Experimental operating conditions.

λ [-]	Rotor rotational velocity [rad/s]	U_∞ [m/s]	C_t [-]
4.8	60.8	3.8	0.82
6	113.1	5.7	0.89

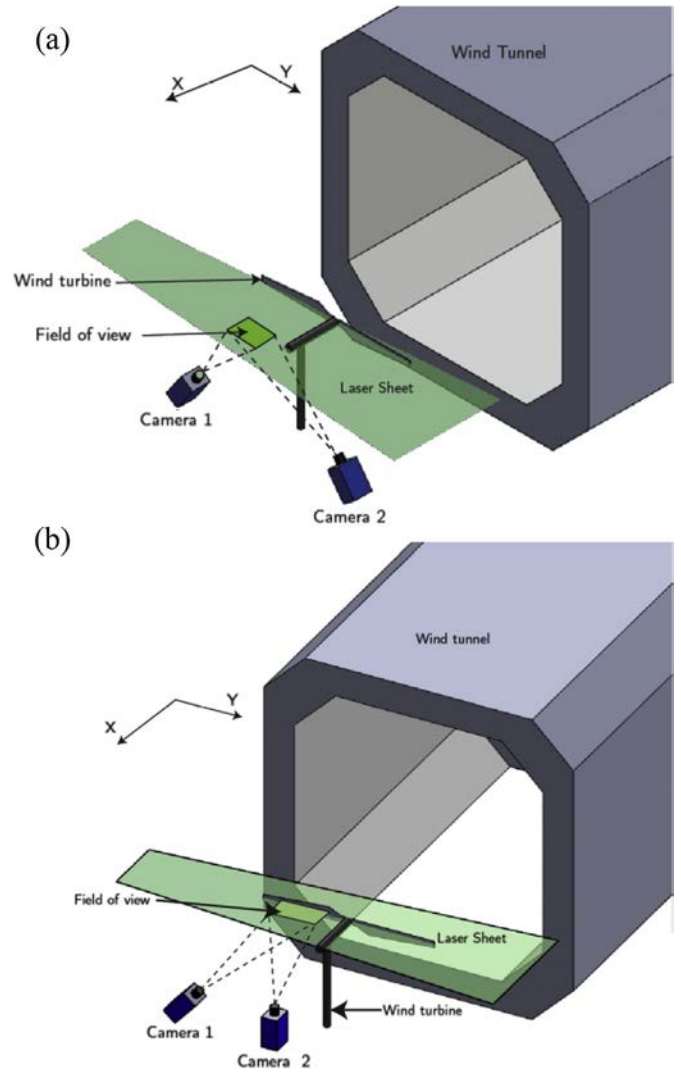


Fig. 6. Schematic of the experimental set-up for wake measurements (a) and measurements at rotor location (b).

obtained from hotwire measurements and presented in Section 2.4. The employed model is a two-bladed horizontal-axis wind-turbine shown in Fig. 1, with design tip speed ratio $\lambda = 6$ and a rotor diameter $D = 0.6$ m (radius $R = 0.3$ m). The wind-tunnel blockage-ratio is 0.04. The rotor blades have a maximum twist of 19.4° at the root and a minimum twist of 4.4° at the tip. The maximum chord of the blade is $c/R = 0.247$ at $r/R = 0.018$ from the blade axis. An Eppler E387 [15] airfoil with a thickness to chord ratio of 9.06% is used along the blade span. The chord-based Reynolds number at the tip region is approximately $Re = 100,000$ at $\lambda = 6$. The C_t - α curves of the E387 airfoil are taken from the reports of [19] and are shown in Fig. 2 for a range of Reynolds number from $Re = 6 \times 10^4$ to $Re = 3 \times 10^5$. The main design drivers, apart from safety and structural integrity, were three. The first was constant circulation along the blade span at the design tip-speed ratio in order to have most of the vorticity trailed only at the tip and at the root with no trailed vorticity in other blade locations. The second was to achieve attached flow conditions over the entire span, which led low angles of attacks and low lift coefficients and therefore to a large average chord. The third requirement was to keep the Reynolds number as large as possible, which also led to large chords and high rotational

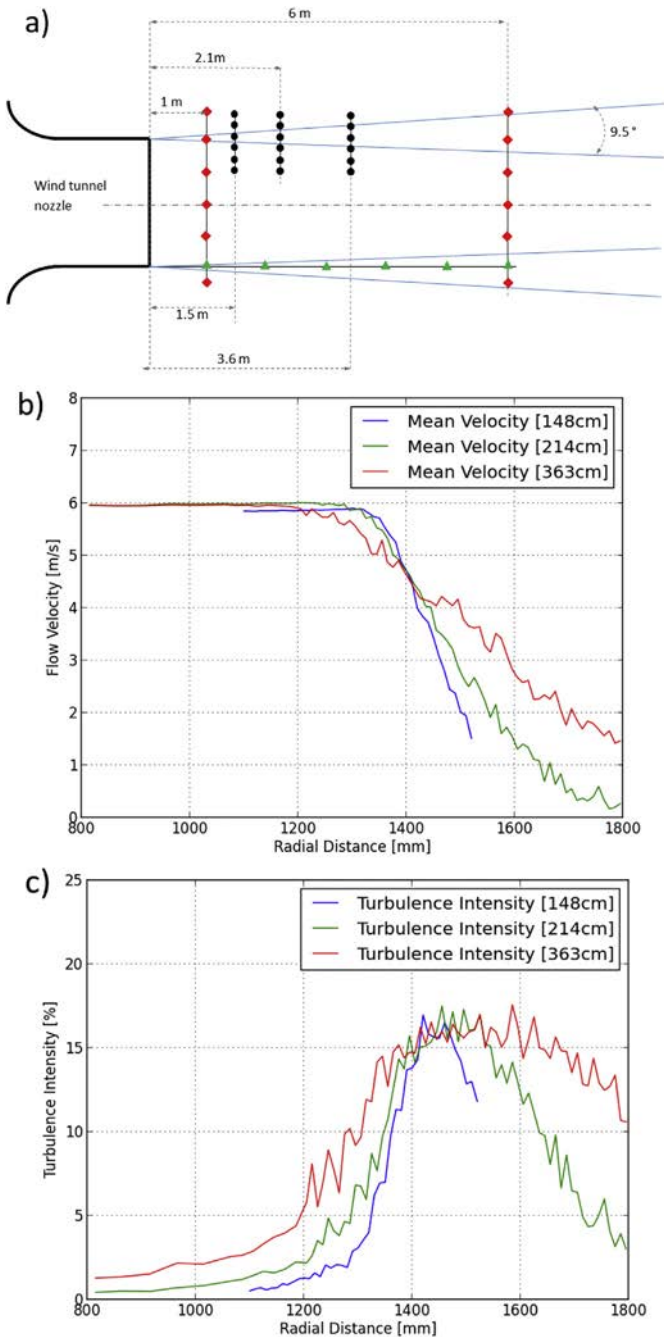


Fig. 7. Wind tunnel jet schematics with measurement points (a). Velocity profiles (b) and turbulence intensity profiles (c) in the radial direction (black points in Fig. 7a) at three different streamwise locations.

speed. The blade's twist and chord distribution are shown in Fig. 3. The nacelle is designed to reduce to minimum its impact on the flow while housing a DC brushless motor, a gearbox, a hall-encoder and an optical trigger (opto-coupler TCST 2103) which provides a one pulse per revolution signal allowing for the PIV synchronization; the nacelle has a diameter of 0.038 m (6.3% of the rotor diameter).

2.2. Thrust force measurements

The performance characterization of the wind turbine is obtained by measurement of the thrust coefficient for different

tip-speed ratios placing the turbine on an external 6-components balance. The balance is $0.522 \times 0.595 \text{ m}^2$ structure onto which the entire wind turbine tower can easily be mounted. The device is provided with six load cells (or Wheatstone bridges) which are able to measure three components of force, in the axial (F_x), radial (F_y) and vertical (F_z) directions, and three components of moment, in the rolling (M_x), pitching (M_y) and yawing (M_z) directions as indicated in Fig. 4, where BC indicates the centre of the balance. For the present thrust measurements, only the axial force component has been recorded.

To measure the thrust at different tip-speed ratios, the wind-tunnel speed and the turbine rotational frequency have been varied. The range of measured tip-speed ratios spans from $\lambda = 2$ to $\lambda = 8$. In order to correct the data for tower and nacelle effects, the axial force acting on the tower and the dummy clean nacelle with no blade has been recorded for the same range of tip-speed ratios and then subtracted from the results of the full turbine measurements. The C_t - λ characteristic of the turbine is shown in Section 3.1.

2.3. Stereoscopic PIV equipment

A stereoscopic PIV setup has been installed on a traversing system able to scan the flow field in the wake of the horizontal-axis wind-turbine model. The required illumination is provided by a Quantel Evergreen Nd:YAG laser system with 200 mJ/pulse energy at a max frequency of 15 Hz (527 nm wavelength). The laser light is conveyed to form a 2 mm laser sheet of about 0.35 m width at the field of view, by combination of a spherical lens of focal $f = -50$ mm and two cylindrical lenses of $f = +80$ mm and $f = -40$ mm. Two LaVision Imager Pro LX 16 Mpix ($4870 \times 3246 \text{ px}^2$, 12 bits) with a pixel pitch of $7.4 \mu\text{m}/\text{px}$ are used to image a field of view of $357 \times 253 \text{ mm}^2$ (corresponding to 0.56×0.42 diameters), obtained with two Nikon lenses of $f = 180$ mm and aperture $f\# = 2.8$ -4, at a magnification M of 0.10. The focusing plane has been slightly offset with respect to the laser plane (defocusing), to obtain an image of the particle of about 2–3 px, to mitigate bias errors associated with peak-locking as shown by Ref. [25]. Seeding particles were injected in the test-section with a SAFEX smoke generator employing a SAFEX MIX, able to produce liquid droplets of less than $1 \mu\text{m}$.

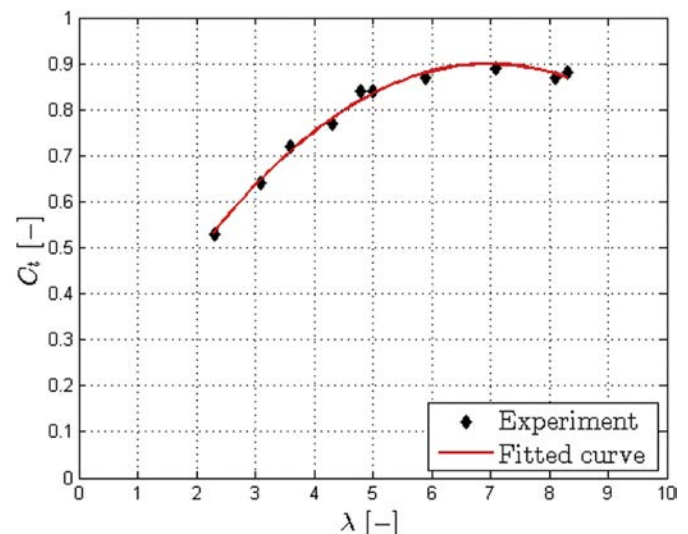


Fig. 8. C_t - λ curve of the wind-turbine model.

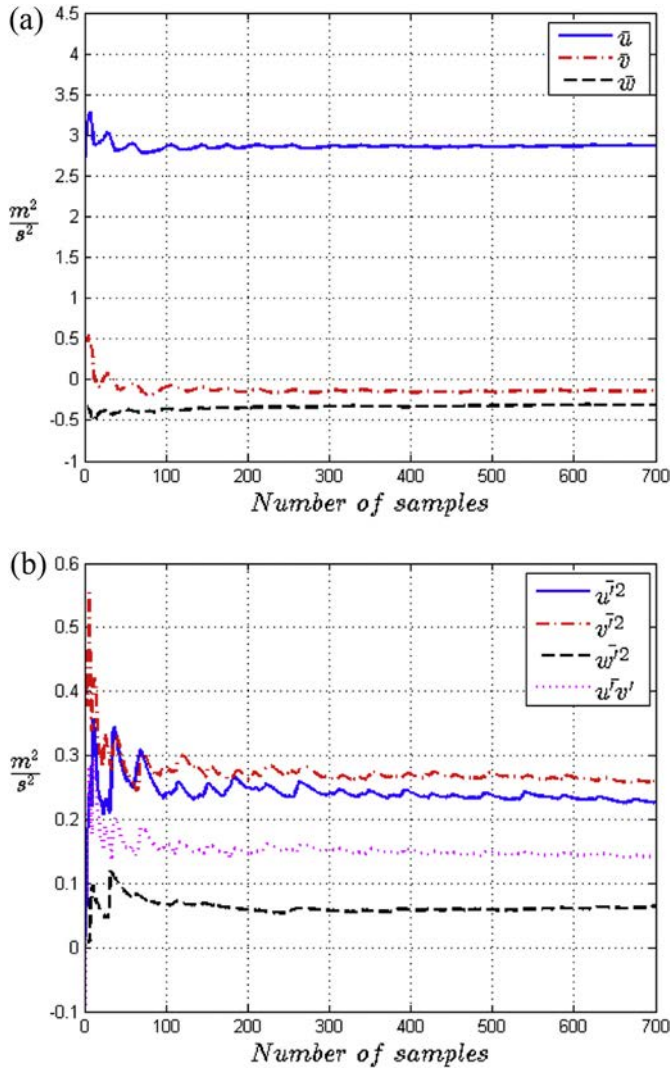


Fig. 9. Evolution of the statistical average velocity (a) and Reynolds stresses (b). Unconditioned sampling.

Ensemble of 400 (phase-locked), 720 (unconditioned) double-frame recordings have been acquired and processed by LaVision Davis 8.1.4. Interrogation windows of $24 \times 24 \text{ px}^2$ with 50% overlap allow to have resolution of 1.76 mm (2.9×10^{-3} diameters), and a vector pitch of 0.88 mm (1.5×10^{-3} diameters), which yields to 404×270 vectors per FOV. The laser control, camera synchronization, and image acquisition are triggered at a prescribed delay from the one pulse signal obtained by the optocoupler TCST 2103.

2.4. Velocity fields configuration

The measurements were performed on the wake of the wind turbine model up to 5 rotor diameters downstream, in multiple fields of view (FOV) at hub height. The positions of the fields of view are represented in Fig. 5, where each squared window represents a field of view (FOV) in the radial plane. The darker shade between the windows shows the overlap between two adjacent FOV, which varies from 0.097 m to 0.147 m (0.16–0.25 diameters) in the axial direction. Two different configurations were employed at two inboard positions with an overlap of 0.102 m–0.098 m respectively (0.17–0.16 diameters).

Measurement phase-locked with the blade motion have been obtained for three different phases of rotation: -5° , 0° and 5° . The distance between the turbine and the wind tunnel exit is approximately 0.5 rotor diameters. This distance is chosen in such a way to maximize the visualization of the wake given the free-expansion of the wake with no wind-tunnel interference. Table 1 summarises the parameters of the two considered test cases with $\lambda = 4.8$ and $\lambda = 6$. The schematics in Fig. 6 show the different position of cameras and laser of the different sets of measurements.

2.5. Wind-tunnel flow characterization

The flow quality of the OJF wind-tunnel has been assessed prior to the acquisition of the wake measurements. A constant temperature hot-wire anemometer (HWA) and a static Pitot tubes have been employed to monitor the mean velocity and turbulence intensity along the jet. Results from the mean velocity profile in the radial direction at 1 m and 6 m from the tunnel nozzle (red squares in Fig. 7a) show relatively good uniform flow respectively within 1% and 3% at 1 m and 6 m from the jet. With a HWA sampling rate of 10 kHz and a sampling time of about 60 s the measured turbulence

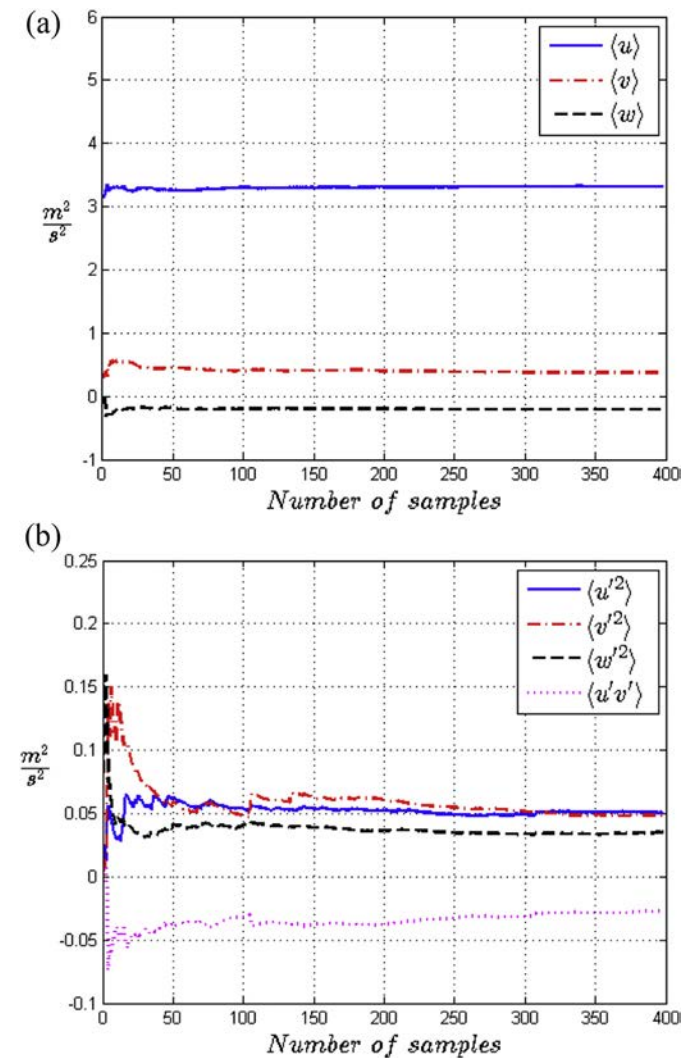


Fig. 10. Evolution of the statistical average velocity (a) and Reynolds stresses (b). Phase-locked sampling.

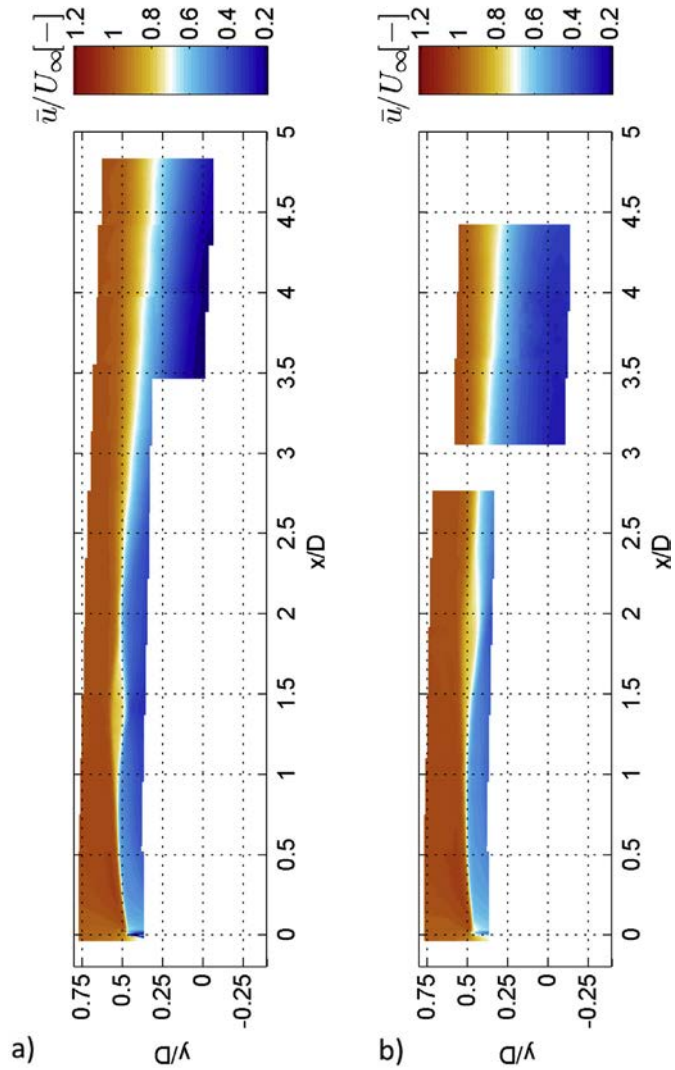


Fig. 11. Unconditioned average axial velocity field \bar{u}/U_∞ in the wake shear layer at $\lambda = 6$ (a) and $\lambda = 4.8$ (b).

intensity is lower than 0.5% at 1 m from the nozzle and lower than 2% at 6 m from the nozzle. A second series of measurements with a sampling rate of 10 kHz and a sampling time of 10 s have been used to calculate the shear layer thickness in the radial direction at 1.5, 2.1 and 3.6 m from the nozzle (black dots in Fig. 7a). Results show an angle aperture of 9.5° for the shear layer. The starting point of the shear layer is assumed at $u/U_\infty R = 98\%$, giving a free-stream area reduction of 16.7 cm/m corresponding to a usable area (namely the area with uniform velocity $u = UR_\infty$) of $2 \times 2 \text{ m}^2$ at 6 m from the nozzle. Fig. 7b and c show the velocity and turbulence profile at three locations within the measurement region of the present experiments. A last series of measurements was performed along the streamwise direction inside the jet shear layer (green triangles in Fig. 7a) with a sampling rate of 10 kHz and a sampling time of 10 s for checking the stability of the jet. Results from Fast Fourier Transform analysis of the velocity time series show highly energetic fluctuations at low frequency. The frequency of these oscillations is clearly dependent on the flow Reynolds number. At a velocity of 6 m/s, the energy spectrum shows peaks at $1.1 \pm 0.1 \text{ Hz}$ and at $1.9 \pm 0.1 \text{ Hz}$ at 8 m/s in each streamwise location. The amplitude of the oscillations after 4 m downstream the wind tunnel nozzle is 1.6% of the mean velocity and becomes higher than

2.8% at after 6 m. The present experiments are performed within a region extending up to 3 m downstream the jet and, radially, up to 0.5 m from the jet centreline, zone with an assessed turbulence intensity of 0.5% and a flow inhomogeneity of less than 1% and free stream velocity fluctuations lower than 1.0%.

2.6. Reynolds number independency

Within the present measurement volume and available equipment the achievable Reynolds number based on the turbine diameter is of the order of $\sim 10P^4 \div 10P^5$, one order of magnitude lower than in full-scale operating conditions. Previous studies have demonstrated that the wake exhibits a low dependency on the Reynolds number [26], compared experimental measurements in the wake of a small wind-turbine with a chord-based Reynolds number ranging from 6400 to 16,000 with results from an inviscid vortex code. Results from the comparison show that the fundamental behaviour of the helical vortex wake is weakly sensitive to Reynolds number, being the numerical results fully comparable with the experimental ones. Further results from the [5] suggest

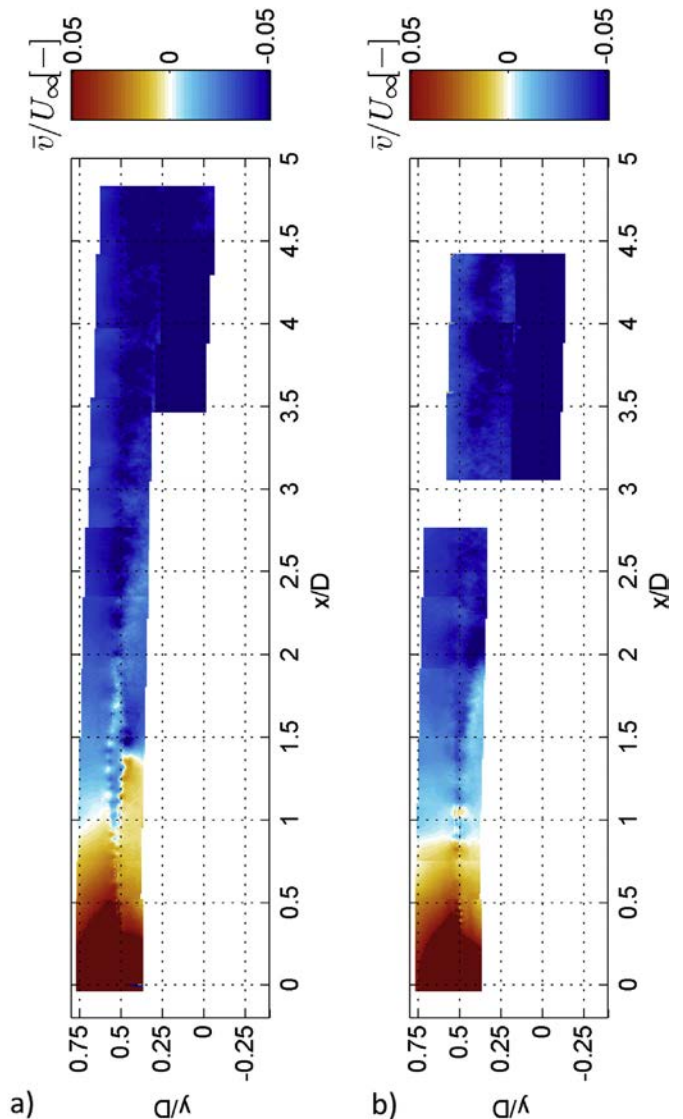


Fig. 12. Unconditioned average radial velocity field \bar{v}/U_∞ in the wake shear layer at $\lambda = 6$ (a) and $\lambda = 4.8$ (b).

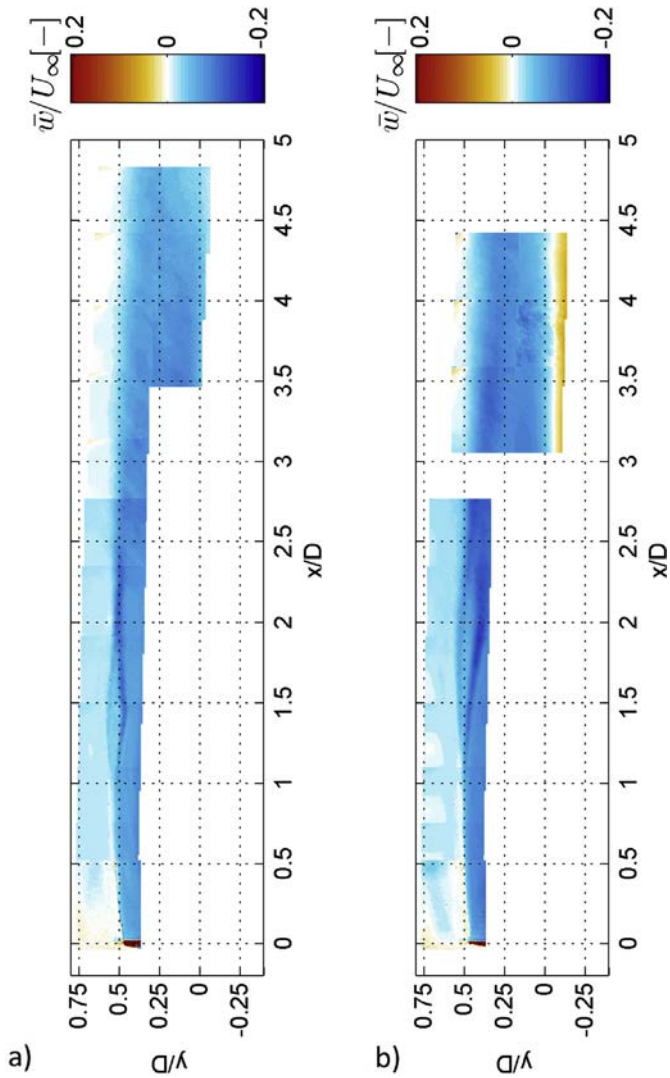


Fig. 13. Unconditioned average azimuthal velocity field \bar{w}/U_∞ in the wake shear layer at $\lambda = 6$ (a) and $\lambda = 4.8$ (b).

that main flow statistics (mean velocity, turbulence intensity, kinematic shear stress and velocity skewness) become independent of Reynolds number from $Re = 9.3 \times 10^4$. In the present study the Reynolds number based on the rotor diameter ranges from $Re = 1.5 \times 10^5$ to 2.3×10^5 sufficiently higher than the critical value estimated by Ref. [5].

3. Measurement results

3.1. Thrust measurements

The results of the thrust measurement are reported in Fig. 8, where black dots indicate experimental data fitted with the red curve. For the design tip-speed ratio $\lambda = 6$ the thrust coefficient is $C_t = 0.89$ as predicted by momentum theory for the design induction factor $a = 1/3$.

3.2. Convergence analysis

Study of the kinetic energy in the wake requires having a converged statistical dataset of the velocity components and their fluctuations. Hence, prior to start the acquisition, a convergence analysis has been performed by acquiring a very large amount of

images in a selected location in the wake and by testing the convergence of the statistics. Figs. 9 and 10 show the unconditioned average plot versus then number of samples acquired of the three mean velocity components and the Reynolds stresses tensor components. About 400 acquisitions guaranteed convergence of the phase-locked mean components, while 700 acquisitions are needed for the unconditioned averages. The values shown in the graphs are obtained at the wake breakdown ($\lambda = 4.8$).

3.3. Global velocity field and wake re-energising

The near- and transition-wake velocity fields until 4 diameters downstream are shown for two different tip-speed ratios. Results are presented for phase-lock and unconditioned averages, namely representing the average of the velocity field corresponding to a prescribed blade phase and the time average flow field. Figs. 11–14 depict the normalized unconditioned average of the velocity field in the shear layer between the wake and the outer flow until about 5 diameters downstream. The contours show the location of the

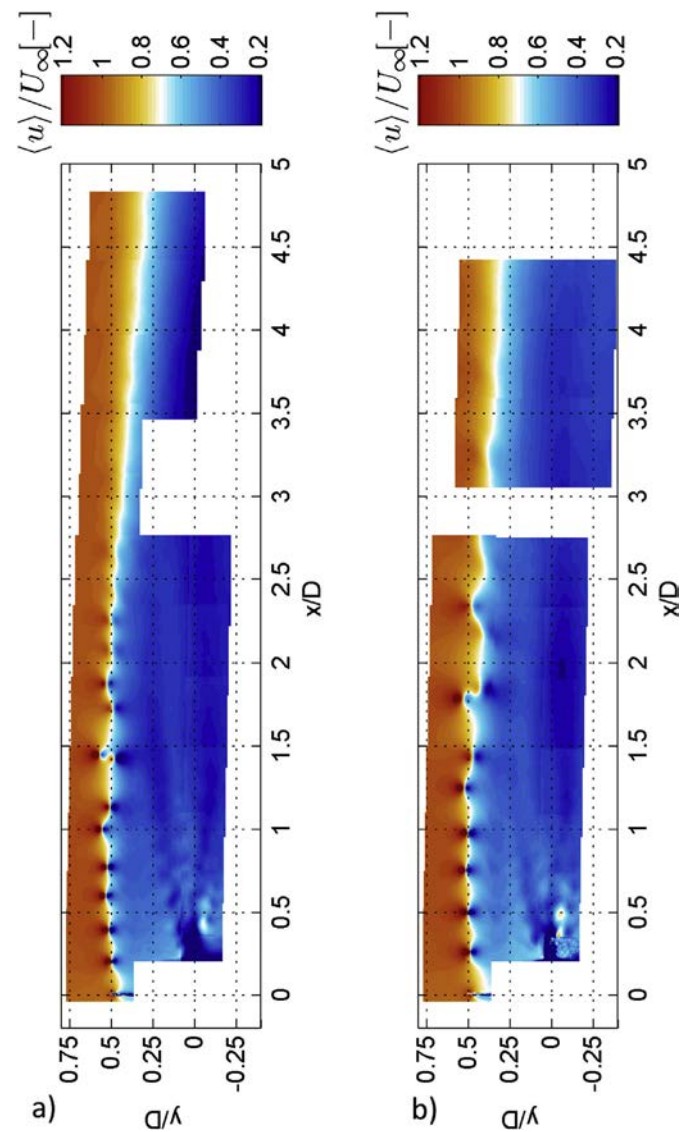


Fig. 14. Phase-locked average axial velocity field $\langle u \rangle / U_\infty$ in the wake shear layer at $\lambda = 6$ (a) and $\lambda = 4.8$ (b).

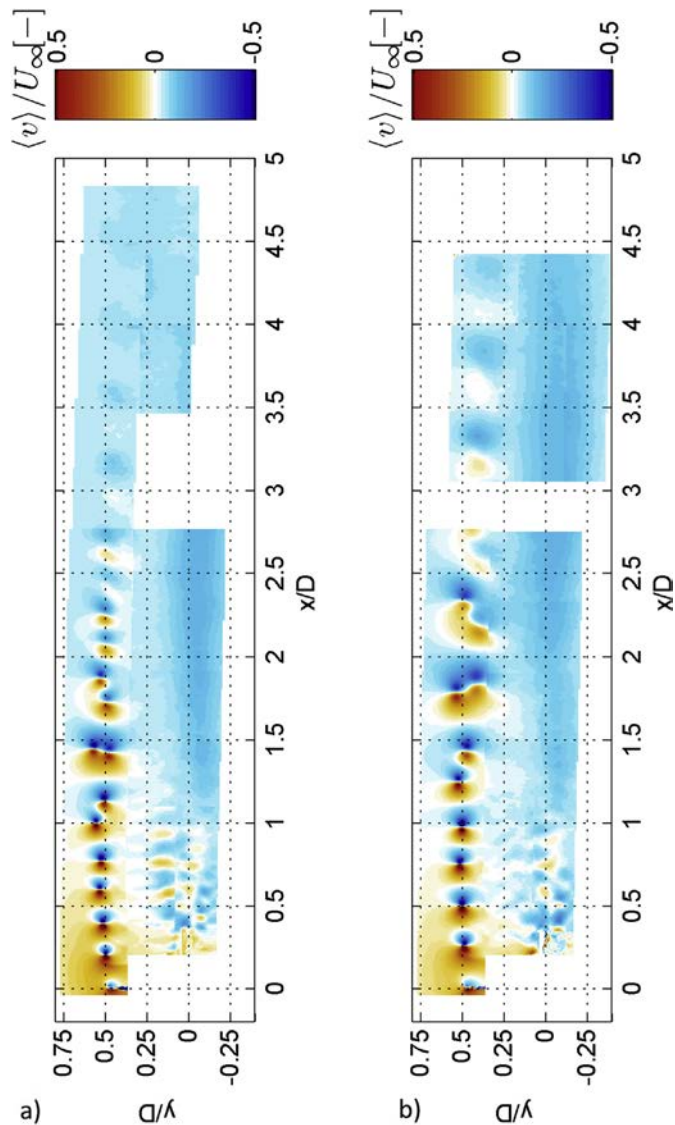


Fig. 15. Phase-locked average radial velocity field $\langle v \rangle / U_\infty$ in the wake shear layer at $\lambda = 6$ (a) and $\lambda = 4.8$ (b).

wake breakdown, due to the vortex pairwise interaction, the so-called leapfrogging, as shown also in Refs. [8] and [11]. In the unconditioned average axial velocity field (Fig. 11), this appears as a sudden enlargement of the shear layer, starting at ~ 1 diameter downstream for $\lambda = 6$ and ~ 1.3 diameters downstream for $\lambda = 4$ and reaching its maximum at ~ 1.4 diameters for $\lambda = 6$ and at ~ 1.7 diameters for $\lambda = 4.8$. The onset of the wake instability is therefore clearly depending on the λ as shown in Ref. [8]. In Fig. 12, showing the unconditioned average radial velocity field, the dependence on the tip-speed ratio is less evident; the most evident feature is an abrupt change of sign of the velocity direction, which becomes negative (namely toward in the inner region of the wake) after about one diameter, already before the onset of the tip-vortex instability. Figs. 14–16 show the phase-locked velocity field of the shear layer and the inboard region until the hub centreline. In Figs. 14 and 15, showing respectively the phase-lock average axial and radial velocity, the evolution of the tip vortex together with its pairwise interaction shows a predominant tip-vortex diffusion after the leap-frogging event. This would suggest a strong influence of the large scale wake instability on the tip-vortex diffusion. This is also very evident in Fig. 16 which depicts the azimuthal velocity

field. Regions of positive velocity mean flow rotating in the same direction of the blades due to the viscous drag (e.g. the tip-vortex cores and the wakes of the blades), whereas negative regions represent counter rotating flow. After the leapfrogging, there is a clear change of sign of the velocity direction inside the tip-vortex. The analysis of such a phenomenon is reserved for future studies. Fig. 17 depicts the span-wise profile of axial velocity at different downstream locations. Data are taken from phase-locked measurements. The red dashed lines represents the value of maximum wake expansion predicted by momentum theory (horizontal line) and the value of minimum wake velocity (vertical line). Theoretical predictions are in rather good agreement with the experimental results as far as the minimum wake velocity estimation is concerned, although the measured wake expansion seems lower than the theoretical one. Another phenomenon is observed: the most downstream profiles exhibit an inversion of the wake expansion. At $\lambda = 4.8$ this is evident at $2.7D$, but at $\lambda = 6$ this already evident at $1.6D$. The hypothesis is that tip-vortex instability has also a sensible effect on the wake expansion process. The strong fluctuations of phase-locked velocity in the near hub region are mainly due to

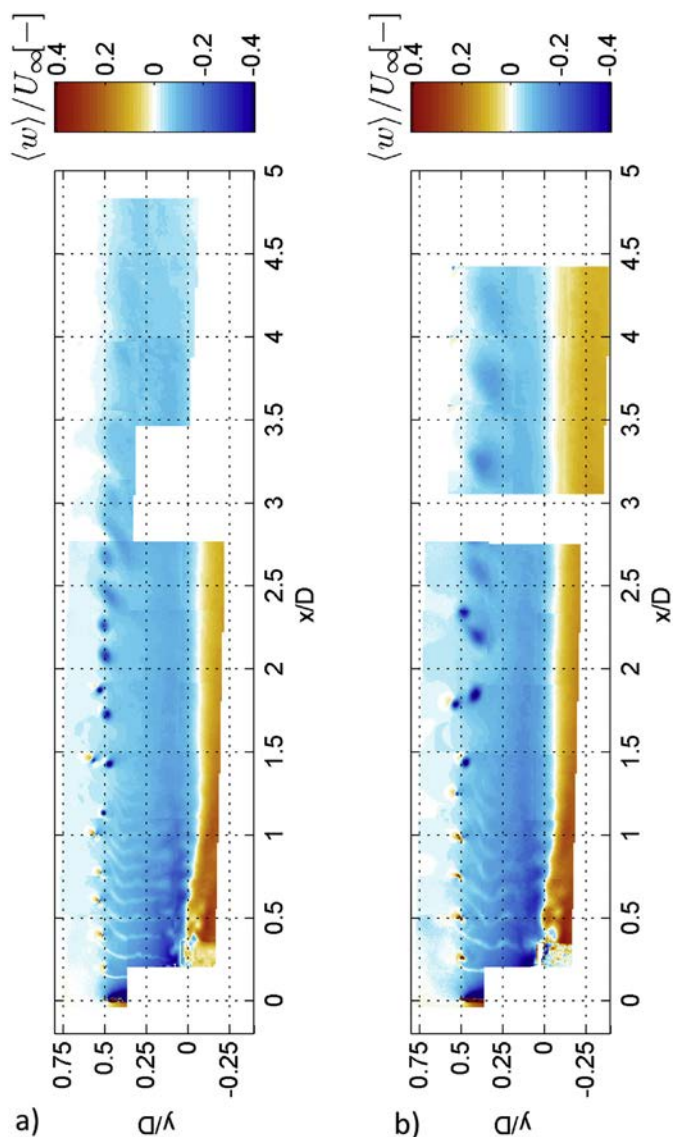


Fig. 16. Phase-locked average azimuthal velocity field $\langle w \rangle / U_\infty$ in the wake shear layer at $\lambda = 6$ (a) and $\lambda = 4.8$ (b).

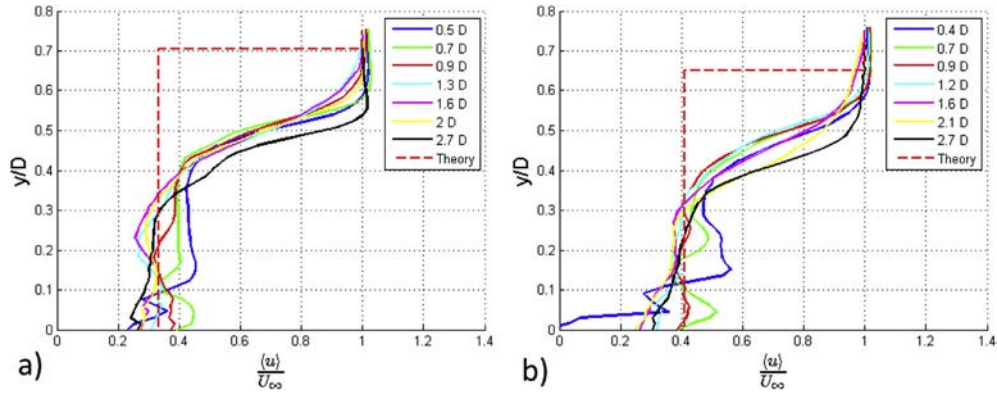


Fig. 17. Vertical profiles of normalized phase locked axial velocity field $\langle u \rangle / U_\infty$ at 7 different downstream locations compared with the momentum theory profile at $\lambda = 6$ (a) and $\lambda = 4.8$ (b).

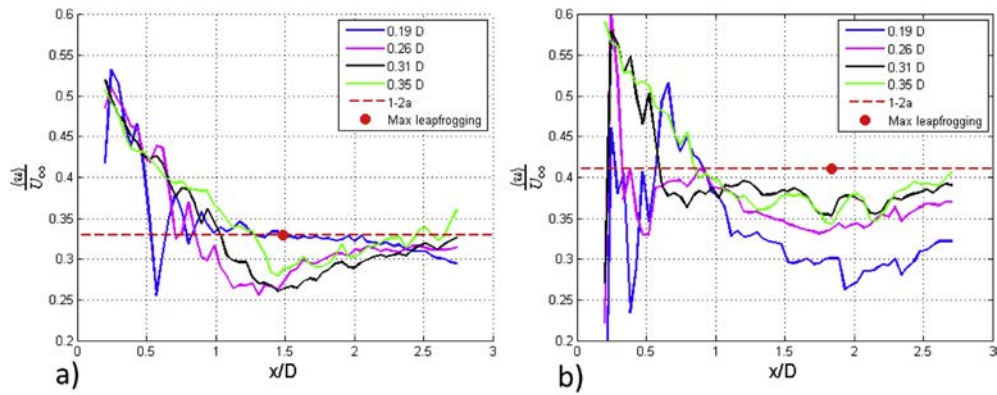


Fig. 18. Stream-wise profiles of normalized phase locked axial velocity field $\langle u \rangle / U_\infty$ at 4 different radial locations compared with the momentum theory value at the maximum wake expansion $u_{\text{wake}} = U_\infty(1-a)$ at $\lambda = 6$ (a) and $\lambda = 4.8$ (b). The red dot indicates the location of the "maximum leapfrogging" in that phase, when the tip-vortices are one on top of each other.

experimental error caused by possible shadowing/reflection from the nacelle and by the presence of the nacelle vortex shedding, which is not in phase with the turbine rotation. Fig. 18, presenting the stream-wise profiles of axial velocity at different radial locations, shows that the re-energising process starts right after the instability around locations ~ 1.4 diameters for $\lambda = 6$ and at ~ 1.7 diameters for $\lambda = 4.8$. Comparing Figs. 18 and 17, it is clear that the onset of the re-energising process coincides with the location of the leapfrogging event (in the graphs, the red dot represent the locations where the vortices are one on top of each other after a 90° revolution and is defined as the "maximum leapfrogging" location). After reaching a minimum at the maximum wake expansion, the axial velocity intakes a process of re-energising, starting from the outer regions where the turbulent mixing with the external flows happens as evident in Fig. 17.

3.4. Vorticity field and tip vortex evolution

In this section, the evolution of the tip vortex is analysed in terms of vorticity. Fig. 20 shows the value of out-of-plane vorticity obtained from the phase-locked average velocity fields. This is obtained with (1):

$$\langle \omega_z \rangle = \frac{\partial \langle v \rangle}{\partial x} - \frac{\partial \langle u \rangle}{\partial y} \quad (1)$$

where u and v are the velocity components parallel to the measurement plane. Results show the strong, concentrated vorticity at the tip-vortices location together with its disruption after the wake instability. Fig. 19 depicts the evolution of circulation and vorticity

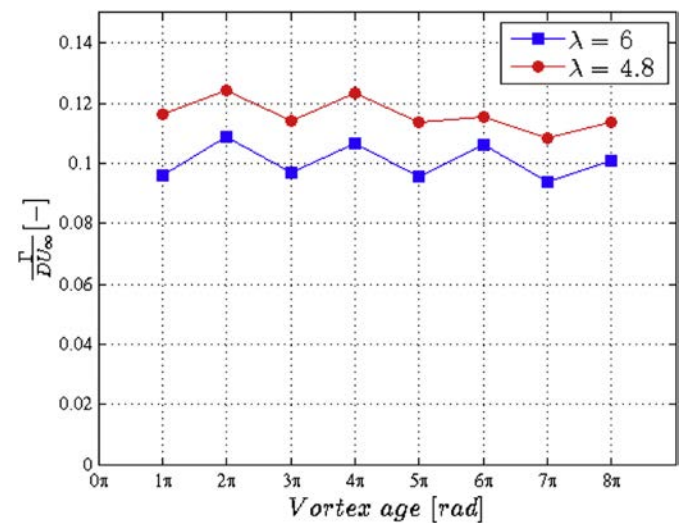


Fig. 19. Evolution of tip vortex circulation Γ as function of vortex age.

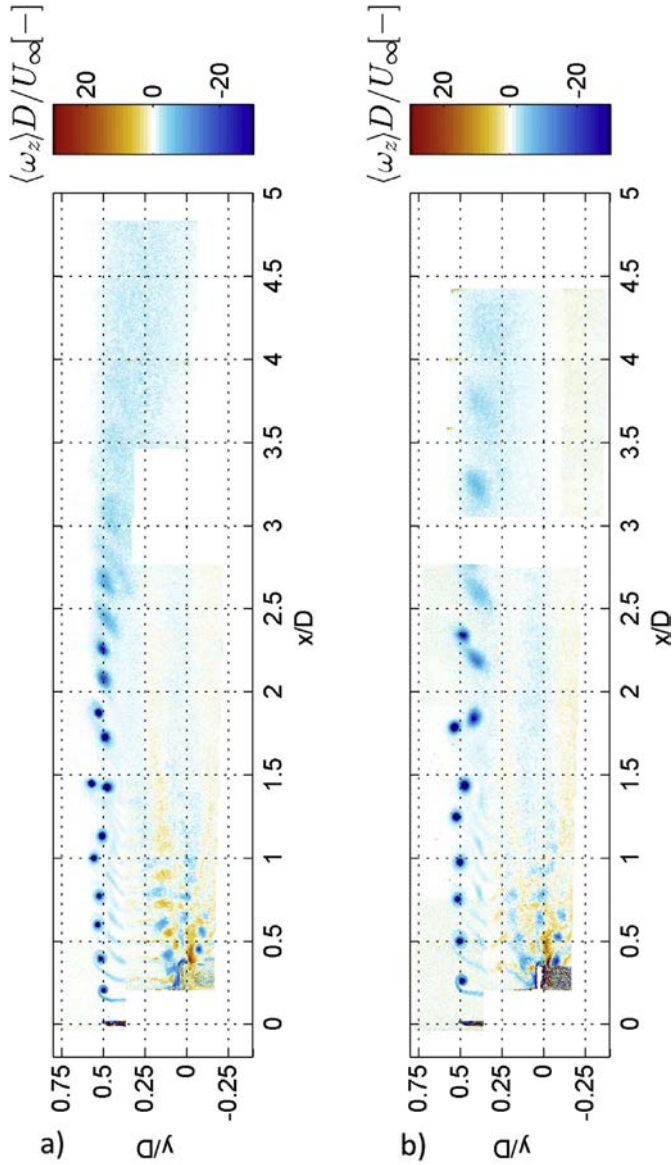


Fig. 20. Phase-locked average out-of-plane vorticity field $\langle \omega_z \rangle D / U_\infty$ at $\lambda = 6$ (a) and $\lambda = 4.8$ (b).

as function of the vortex age. In the two graphs, the vortices from both blades have been considered. The flow circulation has been calculated integrating the velocity along a closed line C containing the vortex. From Fig. 19 it is possible to notice that the vortex released by blade 1 is slightly stronger than the one released by blade 2 in both test cases. The difference is estimated around 6% and it is attributed to experimental error, which most likely derives from small differences in the blade manufacturing. Fig. 21 shows the value of vorticity perpendicular to the field of view obtained from the unconditioned average velocity fields.

$$\bar{\omega}_z = \frac{\partial \bar{v}}{\partial x} - \frac{\partial \bar{u}}{\partial y} \quad (2)$$

Results show that the vorticity is organised as a concentrated sheet which bifurcates at the location where the vortex leap-frogging occur, after which breaks down and diffuses quite rapidly. This is, at least before the wake instability, similar to what it would have been obtained with an actuator disc simulation.

3.5. Wake turbulence

In this section the wake is analysed in terms of turbulence and Reynolds stresses. Fig. 22 shows the phase-lock average x - y component of the shearing stresses $u_s v_s$. This is an important quantity because, as demonstrated by Refs. [1,3,4,9] and [16]; this is related to the vertical transport of momentum, with negative values of shear meaning entrainment into the wake of the free-stream flow momentum and as such directly related to the re-energising process. The phase-lock shearing stresses are calculated with (3)

$$\langle u_{s,i} u_{s,j} \rangle = \frac{\sum_{k=1}^N [u_i(t_{k,\varphi}) - \langle u_i \rangle] [u_j(t_{k,\varphi}) - \langle u_j \rangle]}{N} \quad (3)$$

where $t_{k,\varphi}$ is the sampling time at phase φ , N is the total number of samples and, for the case of the x - y component, $i = 1$ and $j = 2$. Clearly, the phase-lock shearing stresses are associated with the random fluctuations. Two regions can be distinguished. In the near-

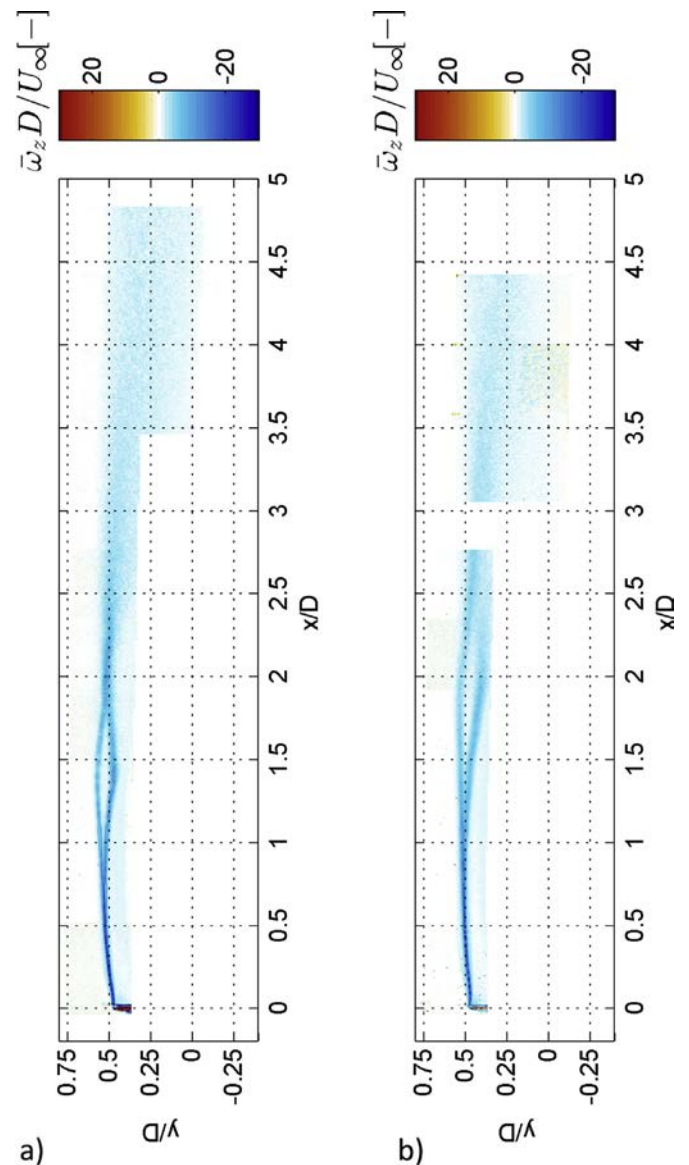


Fig. 21. Unconditioned average out-of-plane vorticity field $\bar{\omega}_z D / U_\infty$ at $\lambda = 6$ (a) and $\lambda = 4.8$ (b).

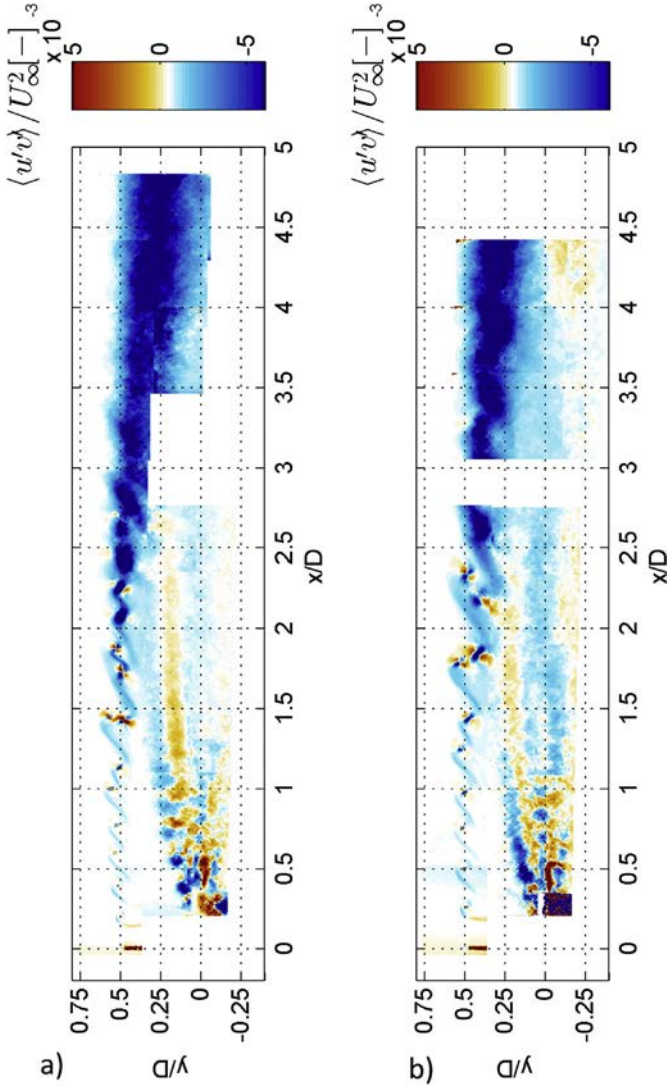


Fig. 22. Phase-locked average x-y component of Reynolds stresses $\langle u_s v_s \rangle / U_\infty^2$ at $\lambda = 6$ (a) and $\lambda = 4.8$ (b).

wake region, the distribution of shearing stresses is strongly influenced by the evolution of the tip-vortex structure, with a concentration of the shearing stresses in the saddle points between two consecutive vortices. This is in good agreement with the findings of [4]; who demonstrated experimentally how the shearing stresses due to the random turbulence have an extreme value near the saddle points between the vortices. This concentrated shear is associated with deep incursions of free-stream fluid into the regions between the vortices. In the region after the instability, the physics of the phenomenon changes radically: after the tip-vortex breakdown, the shearing stresses become suddenly larger and with negative sign, suggesting a more violent mixing, characterised by a strong entrainment of free-stream momentum. In the near-wake region it is also evident the presence of the nacelle's wake and the root vortex as a region with high positive and negative values of $\langle u_s v_s \rangle$, quickly disappearing within less than 2 diameters downstream. Fig. 23 shows the unconditioned average x-y component of the Reynolds stresses $\overline{u'v'}$ calculated with (4):

$$\overline{u'_i u'_j} = \frac{\sum_{k=1}^N [u_i(t_k) - \bar{u}_i] [u_j(t_k) - \bar{u}_j]}{N} \quad (4)$$

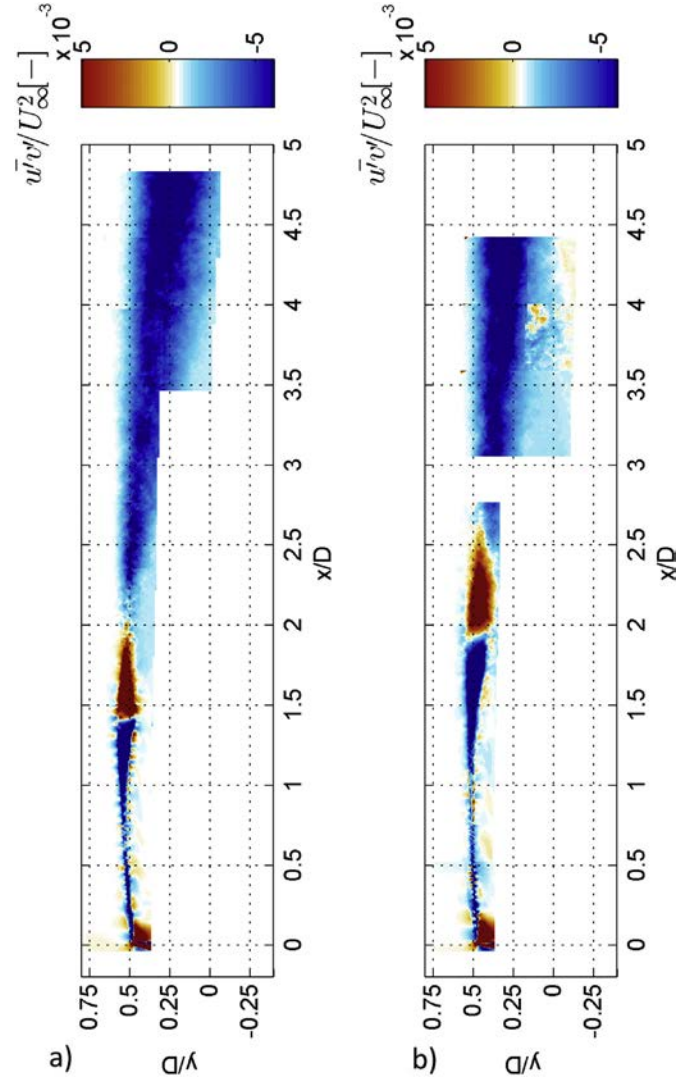


Fig. 23. Unconditioned average x-y component of Reynolds stresses $\overline{u'v'}/U_\infty^2$ at $\lambda = 6$ (a) and $\lambda = 4.8$ (b).

where t_k is the unconditioned sampling time. The unconditioned average shearing stresses are associated with the organised periodic fluctuations. Different regions can be distinguished. In the near-wake region, the shearing stresses are concentrated in a thin sheet at the border of the wake in locus of the vortex cores. In this region, the shearing stresses are characterised by a negative value. In the region where the wake instability occurs, the layer where the shearing stresses are concentrated becomes thicker and, after the location where the tip-vortices completed a 90° orbit around each other, an abrupt change of the shearing stresses sign occurs. After the breakdown of the tip-vortex, the very same behaviour observed in the phase-lock case can be observed.

Fig. 24 shows the turbulence intensity in the shear layer between the inner wake and outer flow relative to the unconditioned average field obtained as $\overline{u}_{RMS}/U_\infty$, where:

$$\overline{u}_{RMS} = \left(\frac{1}{3} \sum_{i=1}^3 \overline{u'_i u'_i} \right)^{0.5} \quad (5)$$

and:

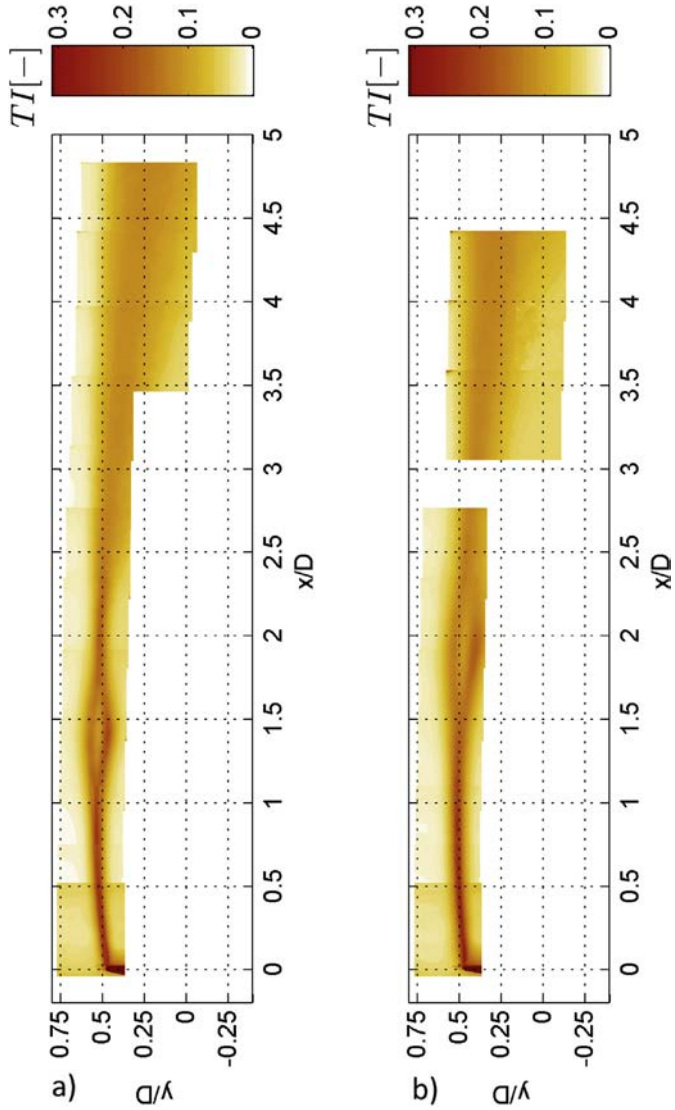


Fig. 24. Unconditioned average turbulence intensity field at $\lambda = 6$ (a) and $\lambda = 4.8$ (b).

$$\overline{u'_i u'_i} = \frac{\sum_{k=1}^N [u_i(t_k) - \bar{u}_i]^2}{N} \quad (6)$$

The high values of TI close to the blades are due to the presence of strong concentrated vortices which are released at the blade tip. In (6) this is accounted for as a flow fluctuation and as such contributes to the total TI . It is evident how the contribution of the organised periodic structures vanishes while travelling downstream. Fig. 25 shows the phase-locked average turbulent intensity in the wake shear layer. This is calculated as $\langle u_{RMS} \rangle / U_\infty$ where:

$$\langle u_{RMS} \rangle = \left(\frac{1}{3} \sum_{i=1}^3 \langle u_{s,i} u_{s,i} \rangle \right)^{0.5} \quad (7)$$

and:

$$\langle u_{s,i} u_{s,i} \rangle = \frac{\sum_{k=1}^N [u_i(t_{k,\varphi}) - \langle u_i \rangle]^2}{N} \quad (8)$$

Results show how the contribution of the random structures become more important and extended in space while travelling downstream, with an opposite behaviour to the contribution of the periodic structures. As last, Figs. 26 and 27 show respectively the unconditioned and phase-locked average turbulence intensity of the x -, y - and z -component (results are presented only for $\lambda = 6$). From Fig. 26 it is possible to appreciate the evident anisotropy of the wake turbulence, where the radial fluctuations are the most important ones, in accordance to previous literature about rotor wake aerodynamics [6,7]. On the contrary, the turbulence anisotropy is not visible in the phase-locked fields shown in Fig. 27.

3.6. Static pressure and total enthalpy

The pressure field is evaluated from the measured PIV velocities to evaluate the transfer of kinetic energy due to the flow pressure in equation (9). The derivation of the pressure from PIV data has been extensively addressed in many fields of research,

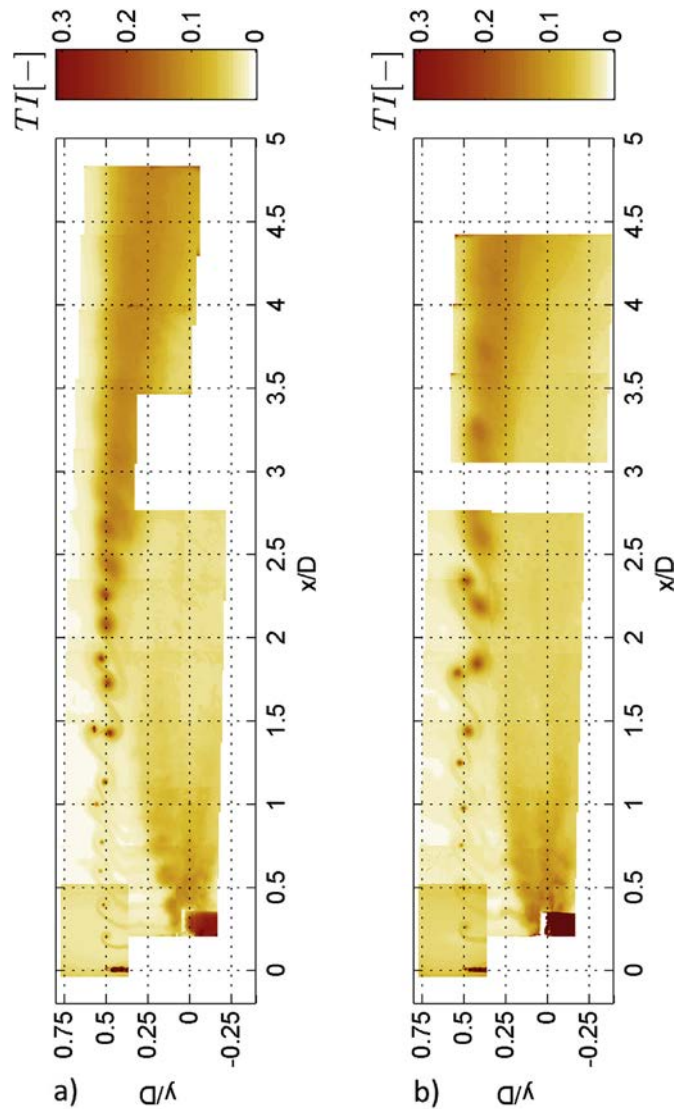


Fig. 25. Phase-locked average turbulence intensity field at $\lambda = 6$ (a) and $\lambda = 4.8$ (b).

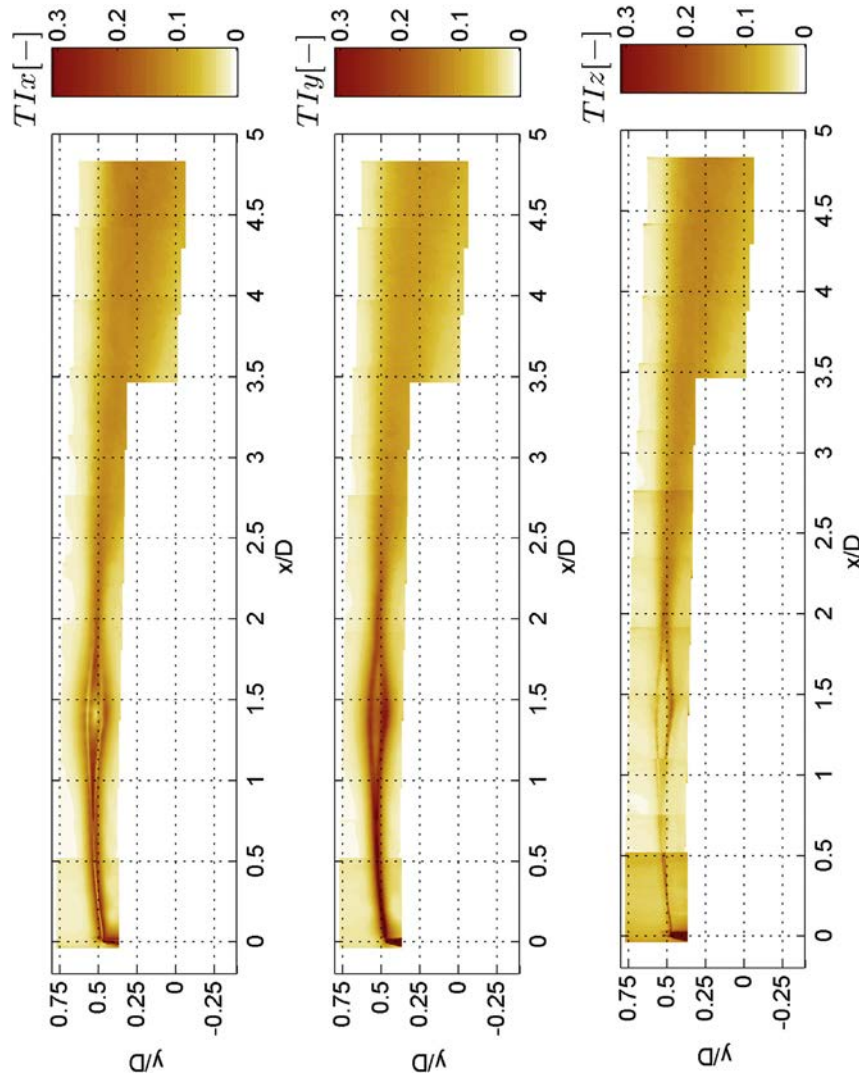


Fig. 26. Unconditioned average turbulence intensity field at $\lambda = 6$ in the three direction: Tlx , Tly and Tlz .

as in Refs. [12,14,15] and [23]. Applications in phase-locked environments for propeller and wind-turbines have allowed reconstructing the 3D periodic pressure fields and subsequently non-intrusively obtaining loads on the turbine blade Ragni et al. (2011) [15]. In irrotational regions, provided that the density is constant in the flow field, the pressure can be approximated by potential flow pressure and computed as a function of the flow velocity according to Bernoulli's equations. In rotational regions, the pressure gradient can still be evaluated from the Navier–Stokes momentum equations, and in presence of viscosity in the flow it reads:

$$\frac{1}{\rho} \frac{\partial p}{\partial x_i} = -\frac{\partial u_i}{\partial t} - u_j \frac{\partial u_i}{\partial x_j} + \frac{\mu}{\rho} \frac{\partial^2 u_i}{\partial x_j^2} \quad (9)$$

where ρ and μ are respectively the flow density and the dynamic viscosity assumed constant. In the present analysis, the volumetric distribution of the velocity gradient tensor is obtained by an Eulerian approach and it is the result of the phase-locked stereoscopic measurements. The time derivative of the velocity is obtained by differentiating the velocity fields at three different phases

(-5° , 0° and 5°). The pressure integration is performed by rewriting the Poisson equation into a 2D Poisson scheme. The pressure integrator used in the present manuscript is based on the version in use by the authors [15]. The algorithm solves the Poisson equation inverting a linear system of equations obtained through a second order finite difference scheme in 2D. Dirichlet (Bernoulli pressure) and Neumann boundary conditions are applied to solve the Poisson equation, depending on the vorticity distribution of the velocity field. The total enthalpy is calculated as in:

$$H = \frac{p}{\rho} + \sum_{i=1}^3 \frac{1}{2} \langle u_i^2 \rangle \quad (10)$$

where p is the static pressure estimated from the PIV velocity field with the method of [15]. Fig. 26 depicts the static pressure coefficient. The tip vortices clearly appear as low pressure zones, whereas in the rest of the wake the pressure is almost constant, apart from the area close to the rotor where a slight negative jump of pressure occurs due to both the wake of the nacelle and the power extraction of the blades. The total enthalpy is normalised

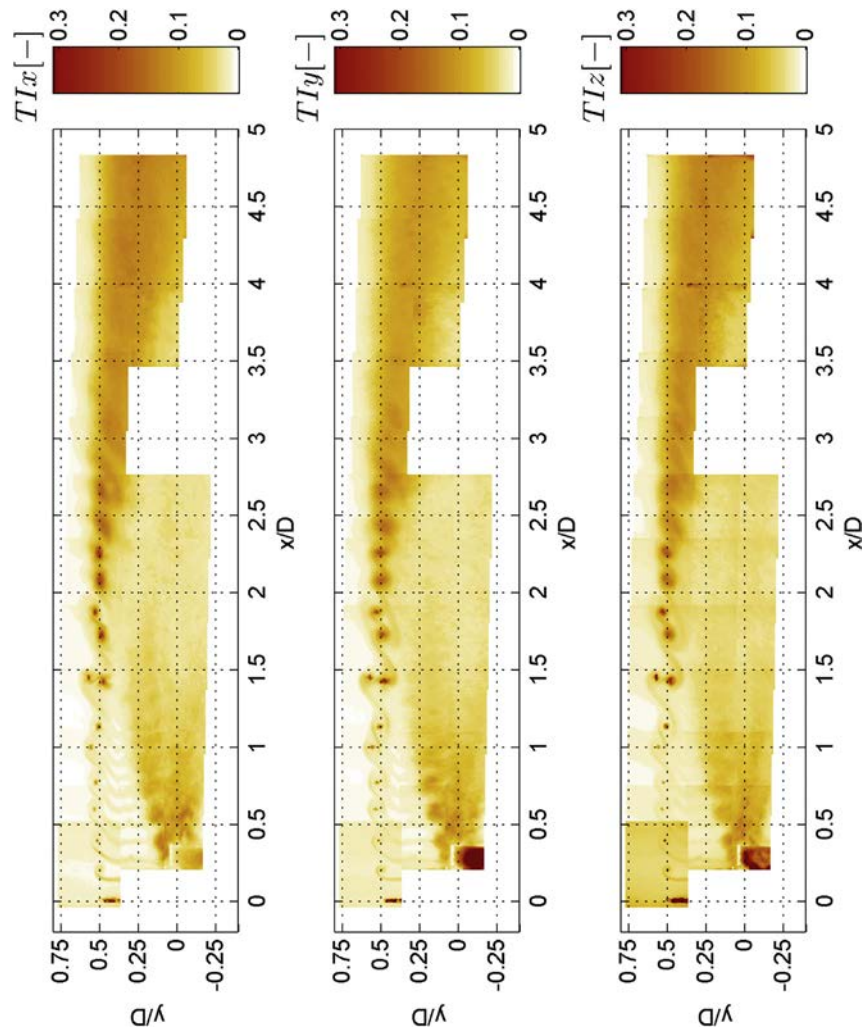


Fig. 27. Phase-locked average turbulence intensity field at $\lambda = 6$ in the three direction: TI_x , TI_y and TI_z .

with the enthalpy of the incoming flow. Fig. 28 shows how the total enthalpy has a completely different behaviour, exhibiting a sudden jump across the shear layer location and a constant value inside the wake region where the wake expansion occurs. In this area in fact the decrease of flow kinetic energy is compensated by an increase of pressure, keeping the value of total enthalpy constant. After the wake expansion and the complete recovery of pressure, the value of H is not constant any longer due to the mixing with the outer flow characterised by a higher kinetic energy.

4. Conclusions

Stereoscopic PIV experiments on a 0.6 m diameter horizontal-axis wind-turbine model have been conducted to study the flow region in the near- and transition-wake. The evolution of the wake flow structures with respect to the tip-speed ratio have been investigated together with the mixing properties of the wake. Analysis of the vortex structure revealed a clear dependency of the wake instability on the rotor tip-speed ratio. The study of the unconditioned average and phase-lock average velocity fields demonstrated how the wake instability affects dramatically all of the flow properties. The time-average

velocity field show a localised enlargement of the wake shear layer in proximity of the tip-vortex instability location. The phase-lock velocity field shows a predominant diffusion of the tip-vortex after the instability, suggesting a direct influence of the large-scale wake behaviour on the tip-vortex diffusive properties. This finding is corroborated by the observation of the azimuthal velocity field, which show a clear change of sign of the velocity direction in the vortex region after the leapfrogging location. Analysis of turbulence statistics demonstrated how the leap-frogging phenomenon has a strong influence on the development of the wake turbulence, leading to a more effective mixing after the location where the instability occurs and the vortex coherence is disrupted. This is also demonstrated by the analysis of the wake axial velocity, together with the pressure and stagnation enthalpy, showing an evident re-energising after the tip-vortex breakdown. The general comparison between the phase-lock and the unconditioned measurements shows that the mixing process after the wake instability is solely dominated by the random motions. Future work is meant to analyse the different terms in the governing equations of the mean flow kinetic energy transport, quantifying the contributions of the periodic and random fluctuations. The results of the present study are made available online for numerical code validation.

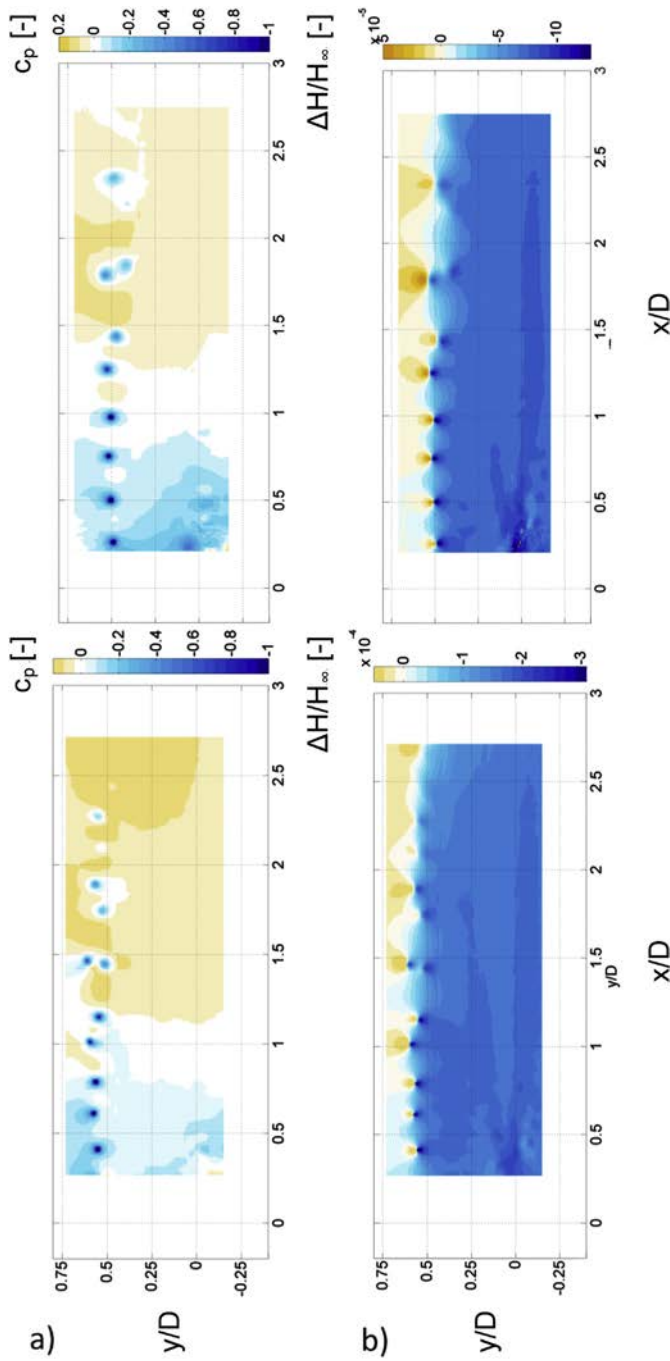


Fig. 28. Phase-locked average pressure field and stagnation enthalpy at $\lambda = 6$ (a) and $\lambda = 4.8$ (b).

Nomenclature

α	angle of attack
λ	tip-speed ratio
μ	dynamic viscosity
ρ	density
φ	phase
ω	vorticity
Γ	circulation
a	induction factor
c	blade chord
C_p	pressure coefficient
p	pressure

r	blade radial location
t	time
x,y,z	axial, radial and azimuthal direction
u_i	i -component of velocity
u_{RMS}	RMS velocity
$\langle u_s, i u_{s,j} \rangle$	Reynolds stresses in the phase-lock field
$\overline{u' i u' j}$	Reynolds stresses in the unconditioned average field
C_t	thrust coefficient
C_l	lift coefficient
D	diameter
H	enthalpy
R	radius
Re	Reynolds number
Tl	turbulence intensity
U_∞	Rfree stream velocity
$\overline{\dots}$	unconditioned average quantity
$\langle \dots \rangle$	phase-lock average velocity

Digital Appendix

The digital annex which is attach to this paper contains all of the results of the present analysis. The results are divided in different folders containing:

- the unconditioned average results for $\lambda = 6$ (shear layer)
- the unconditioned average results for $\lambda = 4.8$ (shear layer)
- the phase-lock average results for $\lambda = 6$ (full wake)
- the phase-lock average results for $\lambda = 4.8$ (full wake)

Each folder contains matrices of

- x - and y -coordinates of the measurement 2D plain
- three components of velocity in the 2D plain u,v and w
- three components of normal Reynolds stressed u^2, v^2 and w^2
- three components of shearing Reynolds stresses uv, uw and vw

More detailed instructions about the contents of the annex and how to read the date are provided in a document contained in the main folder, together with detailed information about the wind turbine model design.

Appendix A. Supplementary data

Supplementary data related to this article can be found at <http://dx.doi.org/10.1016/j.renene.2014.01.020>.

References

- [1] Antonia RA, Chambers AJ, Britz D, Browne LWB. Organized structures in a turbulent plane jet: topology and contribution to momentum and heat transport. J Fluid Mech 1986;172:211–29.
- [2] Barthelmie RJ, Frandsen ST, Nielsen MN, Pryor SC, Rethore PE, Jørgensen HE. Modelling and measurements of power losses and turbulence intensity in wind turbine wakes at Middelgrunden offshore wind farm. Wind Energy 2007;10:517–28.
- [3] Cal RB, Lebrón J, Castillo L, Kang HS, Meneveau C. Experimental study of the horizontally averaged flow structure in a model wind-turbine array boundary layer. J Renew Sustain Energy 2010;2.
- [4] Cantwell B, Coles D. An experimental study of entrainment and transport in the turbulent near wake of a circular cylinder. J Fluid Mech 1983;136:321–74.
- [5] Chamorro LP, Arndt REA, Sotiropoulos F. Reynolds number dependence of turbulence statistics in the wake of wind turbines. Wind Energy 2012;15:733–42.
- [6] Cotroni A, Di Felice F, Romano GP, Elefante M. Investigation of the near wake of a propeller using particle image velocimetry. Exp Fluids 2000;29: S227–36.
- [7] ElKasmi A, Masson C. An extended model for turbulent flow through horizontal-axis wind turbines. J Wind Eng Industrial Aerodynamics 2008;96:103–22.
- [8] Felli M, Camussi R, Di Felice F. Mechanisms of evolution of the propeller wake in the transition and far fields. J Fluid Mech 2011;682:5–53.

- [9] Hamilton N, Kang HS, Meneveau C, Cal RB. Statistical analysis of kinetic energy entrainment in a model wind turbine array boundary layer. *J Renew Sustain Energy* 2012;4:063105–19.
- [10] Hütter U. Optimum Wind-Energy Conversion systems. *Annu Rev Fluid Mech* 1977;9:399–419.
- [11] Ivanell S, Mikkelsen R, Sørensen JN, Henningson D. Stability analysis of the tip vortices of a wind turbine. *Wind Energy* 2010;13:705–15.
- [12] Liu X, Katz J. Instantaneous pressure and material acceleration measurements using a four-exposure PIV system. *Exp Fluids* 2006;41:227–40.
- [13] Medici D. Experimental studies of wind turbine wakes – power Optimisation and Meandering. *Mechanics*. Stockholm: Royal Institute of Technology (KTH); 2005.
- [14] Raffel M, Willert CE, Kompenhans J. Particle image velocimetry: a Practical Guide ; with 24 tables. Springer-Verlag GmbH; 1998.
- [15] Ragni D, Oudheusden BW, Scarano F. Non-intrusive aerodynamic loads analysis of an aircraft propeller blade. *Exp Fluids* 2011;51:361–71.
- [16] Reynolds WC, Hussain AKMF. The mechanics of an organized wave in turbulent shear flow. Part 3. Theoretical models and comparisons with experiments. *J Fluid Mech* 1972;54:263–88.
- [17] Schepers JG. Engineering models in wind energy aerodynamics, Aerospace Engineering. Delft University of Technology; 2012.
- [18] Schepers JG, Van Rooij RPJOM. Analysis of aerodynamic measurements on a model wind turbine placed in the NASA-Ames tunnel. ECN and TUDelft; 2008.
- [19] Selig MS, Guglielmo JJ, Broeren AP, Giguère P. Summary of low-speed airfoil data. Virginia Beach, VA: SoarTech Publications; 1995.
- [20] Sforza PM, Sheerin P, Smorto M. Three-dimensional wakes of Simulated wind turbines. *AIAA J* 1981;19:1101–7.
- [21] Sorensen JN. Instability of helical tip vortices in rotor wakes. *J Fluid Mech* 2011;682:1–4.
- [22] Stevens RJAM, Gayme DF, Meneveau C. Effect of turbine alignment on the average power output of wind-farms. In: Proceedings of the ICOWES2013 Conference; 2013.
- [23] van Oudheusden BW. PIV-based pressure measurement. *Meas Sci Technol* 2013;24:032001.
- [24] Vermeulen PEJ. Mixing of Simulated wind turbine wakes in turbulent shear flow: report. Hoofdgroep Maatschappelijke Technologie TNO; 1979.
- [25] Westerweel J. Fundamentals of digital particle image velocimetry. *Meas Sci Technol* 1997;8:1379–92.
- [26] Whale J, Anderson CG, Bareiss R, Wagner S. An experimental and numerical study of the vortex structure in the wake of a wind turbine. *J Wind Eng Industrial Aerodynamics* 2000;84:1–21.